(Received 12 May 2025, Accepted 17 June 2025, Scheduled 29 June 2025)

Quasi-Z-Source Composite Voltage Vectors Model Predictive Control with a Novel Sliding Mode Reaching Law for PMSM

Yang Zhang[1,*], Yang Gao[1], Kun Cao[1], Ping Yang[1], Gao Tang[1], and Bing Luo[2]

[1] *Hunan University of Technology, Zhuzhou 412007, China*
[2] *CSG Electric Power Research Institute Co. Ltd, Guangzhou, Guangdong Province, China*

ABSTRACT: The model predictive control (MPC) for quasi-Z source inverter (QZSI)-based permanent magnet synchronous motor (PMSM) system suffers from the problems of inductor current ripple, large motor stator current pulsation, and system susceptibility to load torque disturbance. A QZSI composite voltage vector model predictive current control strategy with a novel sliding mode reaching law (CVVs-NSMRL-MPCC) is proposed. Firstly, a composite voltage vector — including one shoot-through, one zero, and two active voltage vectors — is applied to the QZSI during each sampling period, which can effectively reduce the QZSI inductor current ripple and three-phase current pulsation. And the design work for weighting coefficients in the cost function is simplified by calculating the inductor current at ST duty cycle using dead beat control. Furthermore, a sliding mode controller with a novel reaching law is designed for the motor speed loop. Based on it, the external load disturbances are feed-forward compensated to the output port of the controller by the disturbance observer, which reduces the PMSM speed loop pulsation during load torque disturbances and improves the system transient control performance. Finally, the practicality of the strategy proposed in this paper is verified by experiments.

1. INTRODUCTION

Z-source inverter (ZSI) represents a groundbreaking advancement in power conversion topology, effectively addressing the inherent limitations of conventional voltage-source inverters (VSIs) and current-source inverters (CSIs) through the innovative incorporation of a unique LC impedance network. Distinct from traditional converter architectures, ZSI topology enables simultaneous conduction of upper and lower switching devices in the inverter bridge during shoot-through (ST) states, thereby eliminating the necessity for dead-time compensation. This feature enables single-stage voltage boosting by precisely controlling the shoot-through duration [1]. Subsequent developments by Peng's group introduced quasi-Z-source inverter (QZSI) as a topological improvement which demonstrated enhanced performance characteristics, including superior voltage gain, simplified control implementation, and improved dynamic response capabilities for grid disturbance mitigation and load variation accommodation [2, 3]. Quasi-Z-source inverter technology provides notable operational benefits, particularly in maintaining continuous input current and reducing capacitive voltage stress — essential features for improving reliability in high-power energy conversion systems. However, such advantages come at the cost of expanded system dimensions and heightened control intricacy. In [4], to mitigate these limitations, a comprehensive small-signal model for the QZSI is established, and enhanced space vector pulse width modulation (SVPWM) strategies are proposed, with experimental verification of the topology's adaptability in renewable energy systems under dynamic operating conditions. Recent topological innovations, including cascaded QZSI architectures and capacitor-optimized impedance networks, further address scalability challenges by minimizing passive component volumes while boosting power density and efficiency [5, 6]. These advancements have propelled QZSI adoption across critical energy sectors, with demonstrated applications in grid-connected photovoltaics, wind power stabilization, and hybrid electric vehicle drivetrains [7–9].

Finite control set model predictive control (FCS-MPC) exhibits intrinsic strengths in power electronics applications through intuitive implementation, computational efficiency, and flexible multi-objective coordination [10]. Its capacity to achieve high-precision control while managing multiple system variables has driven broad adoption in power converter regulation and motor drive systems [11–14]. A comprehensive review in [15] evaluates FCS-MPC methodologies by analyzing predictive modeling, cost function design, and optimization mechanisms, highlighting critical limitations in parameter sensitivity and computational demands. Proposed research directions focus on advancing permanent magnet synchronous motor (PMSM) drive applications. To overcome challenges of parameter dependency, computational complexity, and variable switching frequency, recent studies have developed integrated solutions with real-time parameter identification, vector preselection techniques, and adaptive weighting strategies [16, 17]. Integration of model predictive control (MPC) with QZSI topologies demonstrates enhanced harmonic suppression and computational efficiency. Advanced implementations leverage improved prediction horizon management to simultaneously reduce total current harmonic distortion (THD) and computational latency [18].

* Corresponding author: Yang Zhang (459387623@qq.com).

A streamlined FCS-MPC approach for RL-load (resistive inductive load) QZSI systems in [19] employs simplified cost functions and vector pre-screening to maintain control fidelity with reduced processor workload. Now, the MPC approach has been further extended to QZSI-based PMSM drive control. Ref. [20] proposes a vector selection strategy using predicted current vector analysis. Candidate voltage vectors are filtered according to angular relationships between three-phase positive-sequence α-axis projections and reference currents. Resulting voltage vector durations determined through modulation techniques demonstrate effective reduction of QZSI inductor current and capacitor voltage ripple. However, this approach introduces elevated ST frequencies that proportionally increase switching losses. Torque ripple reduction is achieved through a cascaded control architecture integrating voltage regulation and switching sequence optimization, as demonstrated in [21]. This dual-mechanism strategy ensures precise tracking of inverter input voltage references through closed-loop regulation while suppressing q-axis current oscillations via an optimized space vector modulation (SVM) algorithm. However, the required supplementary switching network induces non-negligible parasitic power dissipation. In [22], a finite control set model predictive control (FCS-MPC) strategy is proposed for QZSI-PMSM drive systems. This method generates the reference current by synthesizing power compensation values from closed-loop electromagnetic power regulation and capacitor voltage feedback. This synthesis effectively suppresses overshoot and oscillation during capacitor voltage transients and DC-link input disturbances. Ref. [23] proposes a finite-control-set model predictive control (FCS-MPC) strategy with mode-dependent objectives for PMSM drives. In buck mode, control focuses on three-phase currents; in boost mode, it prioritizes inductor current and capacitor voltage regulation. During boost operation, the control architecture implements a dual-stage vector selection: the first sub-cost function evaluates shoot-through voltage vector (STVV) applicability, while the second sub-cost function filters candidate vectors through exhaustive traversal of a subsequent cost function. Compared to unmodulated FCS-MPC, this strategy achieves reduced inductor current and capacitor voltage ripples. However, the dual cost-function implementation inherently increases computational load due to interdependent weighting coefficient coordination. This complexity has motivated focused research on dimensionality reduction strategies for multi-variable weight optimization. A three-phase duty cycle modulation strategy is proposed in [24] for QZSI-PMSM systems, eliminating conventional cost function calculations while maintaining control precision. By coupling control variables across the QZSI and PMSM through inverter bridge arm switching states, the method derives duty cycles from non-singular linear equations and refines them through capacitor voltage error feedback. This method avoids the computational burden of conventional iterative voltage vector screening. It simultaneously mitigates inductor current ripple, capacitor voltage ripple, output current THD, and motor torque pulsation.

A well-documented challenge in MPC applications lies in its inherent sensitivity to parametric variations within controlled systems. Such parametric robustness degradation directly compromises MPC control accuracy, necessitating the thorough investigation of parameter-dependent prediction errors under varying PMSM operational states and QZSI operating conditions [25]. In [26], sensor reduction is achieved through model-based inductor current estimation and capacitor voltage sampling synchronized with current acquisition intervals, significantly minimizing hardware complexity while ensuring measurement accuracy. While effectively minimizing hardware complexity, this approach exhibits elevated output current THD compared to conventional proportional-integral-derivative (PID) control frameworks. A Proportional-Integral-Integral Sliding Mode Control (PI-ISMC) method based on $qd0$ reference system is proposed in [27]. The method achieves asymptotic tracking of the mechanical speed of induction motors under parameter uncertainty and variable load conditions through adaptive optimization of parameters. A model-free predictive control framework is proposed in [28] to address parameter sensitivity challenges in QZSI model predictive control, integrating ST state dynamics through an ultra-local model approach. The methodology constructs unified mathematical representations for resistive-inductive load currents, inductor currents, and capacitor voltages. Experimental validation demonstrates effective transient performance maintenance under parametric mismatch conditions involving QZSI network inductance, capacitance, and load impedance variations. A composite sliding mode control architecture, utilizing PMSM rotational speed and QZSI inductor current as dual state variables, is proposed in [29]. The QZSI-side sliding mode generates ST duty cycles while compensating for system perturbations through a nonlinear observer. Experimental results confirm the strategy's robustness against load speed fluctuations and parameter variations, maintaining stable dynamic responses across operational scenarios.

To address the challenges of inductor current ripple, significant motor stator current pulsation, and load torque sensitivity in QZSI-based PMSM system, a QZSI composite voltage vector model predictive current control strategy with a novel sliding mode reaching law (CVVs-NSMRL-MPCC) is proposed. The key contributions are summarized as follows:

1) A composite VV consisting of STVV, zero VV and two active VVs is applied in a single control cycle to realize the improvement of inductor current ripple and motor stator current waveform distortion rate.

2) ST duty cycle is calculated based on the inductor current dead-beat control, from which inductor current term is thus negligible in the cost function for active candidate VV screening, which simplifies the calibration of weighting coefficients

3) A sliding mode controller with an NSMRL is designed for the speed loop of PMSM, which not only suppresses chattering but also has a faster arrival velocity. Under PMSM transient conditions, speed pulsation is effectively suppressed.

4) Real-time observation of load disturbances in the system is achieved using a disturbance observer, and the observed value is fed forward to the output of the controller, which further improves the anti-interference performance of the PMSM.

TABLE 1. Information corresponding to different VVs of QZSI.

Operating mode	Voltage vectors	Switching state					
		S_1	S_2	S_3	S_4	S_5	S_6
Non-ST mode	V_0	1	0	1	0	1	0
	(zero state)	0	1	0	1	0	1
	V_1	1	1	0	0	0	1
	V_2	1	1	1	0	0	0
	V_3	0	1	1	1	0	0
	V_4	0	0	1	1	1	0
	V_5	0	0	0	1	1	1
	V_6	1	0	0	0	1	1
ST mode	V_7	Simultaneous conduction of the up and down bridge arms switches of any one or more phases					

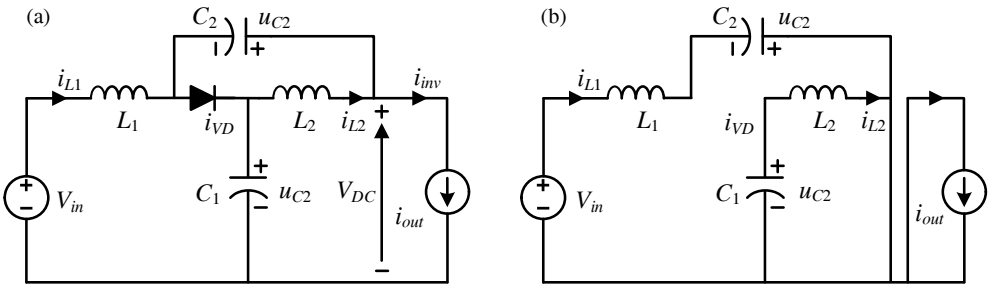

FIGURE 1. Circuit topology of QZSI. (a) Non-ST state. (b) ST state.

The rest of the paper is structured in the following way. In Section 2, QZSI and PMSM mathematical model is established. In Section 3, the design principle and implementation process of CVVs-NSMRL-MPC method is introduced. Experimental results and analysis are given in Section 4. In Section 5, the conclusion section is presented.

2. QZSI AND PMSM MATH MODEL

This section presents the circuit topologies and predictive models of the QZSI network under both ST and non-ST operating states, along with the predictive model of the PMSM.

2.1. Inductance Current and Capacitance Voltage Prediction Model of QZSI

As shown in Table 1, the three-phase QZSI features nine distinct switching states — the eight conventional voltage-source-type inverter states plus a unique ST state. This additional state originates from the QZSI's capability to enable simultaneous conduction of same-phase upper and lower bridge-arm switches.

As shown in Fig. 1, QZSI network has two operating modes: ST and non-ST states.

The dynamic equations for QZSI network i_{L1} and u_{C1} in the non-ST operating mode are:

$$\begin{cases} i_{L1} = i_{inv} + C_1 \dfrac{du_{C1}}{dt} \\ u_{C1} = V_{in} - L_1 \dfrac{di_{L1}}{dt} \end{cases} \tag{1}$$

where V_{in}, u_{C1}, i_{L1} are the voltages of the DC source, voltages of capacitor C_1, current of inductor L_1. i_{inv} is the DC bus current of QZSI network.

$i_{inv}(k+1)$ can be calculated based on the three-phase switching state of the inverter in the next control period and three-phase current at current moment.

$$i_{inv}(k+1) = S_1 i_a + S_3 i_b + S_5 i_c \tag{2}$$

where S_1, S_3, and S_5 represent the three-phase bridge arm switching states of the inverter.

A forward Euler discretization of Eq. (1) is implemented. The prediction equations for $i_{L1}(k+1)$ and $u_{C1}(k+1)$ in the non-ST mode are derived as follows:

$$i_{L1}(k+1) = \frac{T_s\left[V_{in} - u_{C1}(k)\right]}{L_1} + i_{L1}(k) \tag{3}$$

$$u_{C1}(k+1) = \frac{T_s\left[i_{L1}(k+1) - i_{inv}(k+1)\right]}{C_1} + u_{C1}(k) \tag{4}$$

The diode current is interrupted in the ST operating mode. According to the QZSI working principle, the inductor currents and capacitor voltages satisfy $i_{L1} = i_{L2}$ and $u_{C1} = u_{C2}$, respectively, under the symmetric parameter condition $L_1 = L_2$ and $C_1 = C_2$. Analogous to the non-ST mode dynamic equations, the ST-mode dynamics can be expressed as:

$$\begin{cases} L_1 \dfrac{di_{L1}}{dt} = u_{C1} \\ C_1 \dfrac{du_{C1}}{dt} = -i_{L1} \end{cases} \tag{5}$$

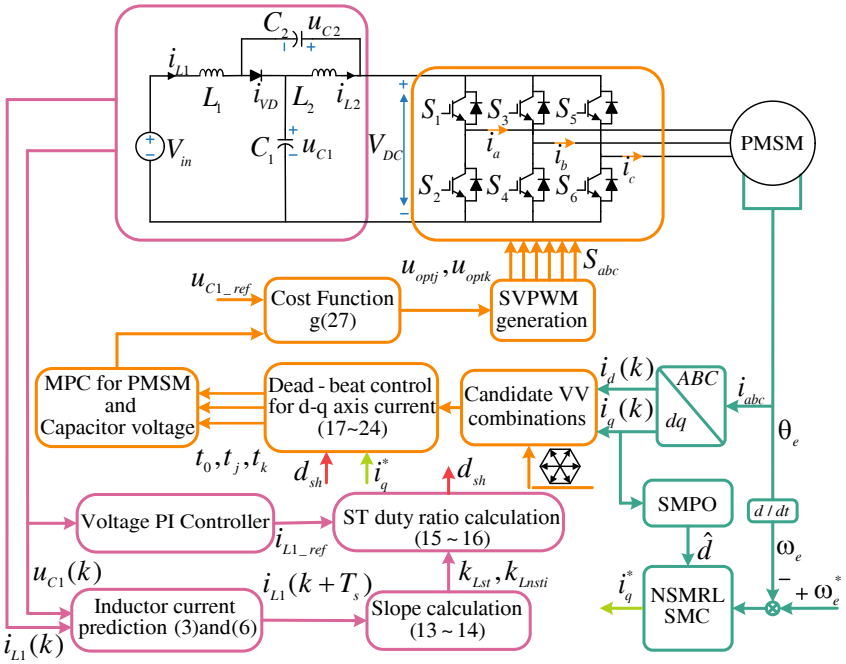

FIGURE 2. The block diagram of the CVVs-NSMRL-MPCC.

A forward Euler discretization of Eq. (5) is performed. The prediction equations for the $i_{L1}(k+1)$ and $u_{C1}(k+1)$ in ST mode are obtained as:

$$i_{L1}(k+1) = \frac{T_s u_{C1}(k)}{L_1} + i_{L1}(k) \tag{6}$$

$$u_{C1}(k+1) = \frac{-T_s i_{L1}(k+1)}{C_1} + u_{C1}(k) \tag{7}$$

2.2. Numerical Modeling of PMSM

The voltage formula of PMSM is built in a two-phase isochronous rotating coordinate system expressed as [30].

$$\begin{cases} u_d = Ri_d + L_d \dfrac{di_d}{dt} - \omega_e L_q i_q \\ u_q = Ri_q + L_q \dfrac{di_q}{dt} + \omega_e L_d i_d + \omega_e \psi_f \end{cases} \tag{8}$$

The electromagnetic torque equation is:

$$T_e = \frac{3}{2} p_n \psi_f i_q \tag{9}$$

where ud, u_q, i_d, i_q, R, ψ_f, ω_e, L_d, L_q, p_n are the dq-axis voltage, dq-axis current, stator resistance, permanent magnet flux linkages, electrical angular velocity, dq-axis stator inductance, number of pole pairs.

The equation of mechanical motion of a PMSM is:

$$J\frac{d\omega_m}{dt} = T_e - T_L - B\omega_m \tag{10}$$

$$\frac{d\theta_m}{dt} = \omega_m \tag{11}$$

where J, B, T_L, and θ_m are the rotor moment of inertia, viscous friction coefficient, load torque, and mechanical torque, respectively.

The prediction formula of dq-axis stator current can be obtained by forward Euler discretization of Eq. (8).

$$\begin{cases} i_d(k+1) = i_d(k) + \dfrac{T_s}{L_s}(u_d(k) - Ri_d(k) + L_s\omega_e(k)i_q(k)) \\ i_q(k+1) = i_q(k) + \dfrac{T_s}{L_s}(u_q(k) - Ri_q(k) \\ \qquad\qquad - L_s\omega_e(k)i_d(k) - \psi_f\omega_e(k)) \end{cases} \tag{12}$$

where $u_d(k)$, $u_q(k)$, $i_d(k)$, $i_q(k)$, $i_d(k+1)$, $i_q(k+1)$, T_s are the dq-axis stator voltages, dq-axis currents at the kth moment, dq-axis currents at the $k+1$st moment, system sampling period.

3. DESIGN OF CVVS-NSMRL-BASED MPCC METHOD

The block diagram of CVVs-NSMRL-MPCC strategy is shown in Fig. 2. In this strategy, the reference value of i_{L1} is generated by the QZSI capacitor voltage proportional-integral (PI) loop, and the reference value of i_q is generated by the speed control PI loop.

3.1. CVVs Based QZSI Control Strategy

From the prediction model of i_{L1}, it can be seen that i_{L1} increases when STVV is applied, while i_{L1} decreases when effective VV and zero VV are applied. As shown in Fig. 3, the quasi-Z-source MPC strategy under conventional SVM strategy applies only STVV and one non-STVV in a single control cycle, resulting in longer charging and discharging cycles and larger current pulsations in i_{L1}. In order to minimize inductor current ripple, dead-beat control of inductor current is realized

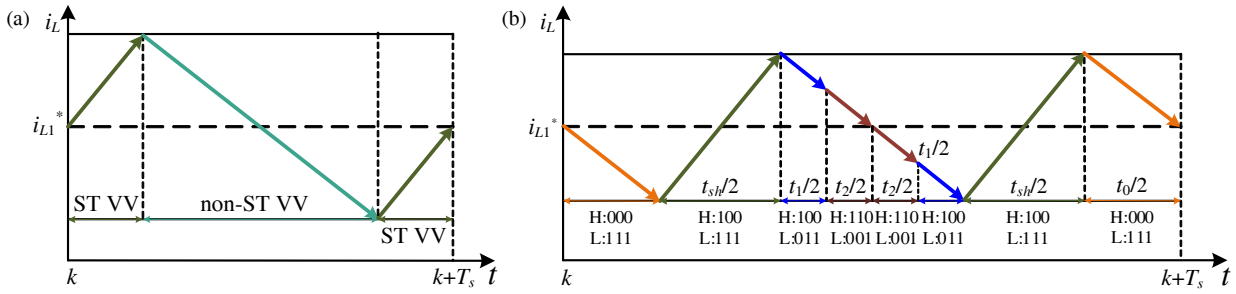

FIGURE 3. (a) i_{L1} of QZSI under conventional SVM strategy (b) i_{L1} of QZSI under CVVs strategy.

through applying a composite voltage vector consisting of four VVs during a single control cycle time, i.e., two effective VVs and zero VVs are applied when $i_{L1} > i_{L1\_ref}$, and the STVV is applied when $i_{L1} < i_{L1\_ref}$. Duration of the action of each VV can be known from ST duty cycle and dead-beat control of dq-axis current.

The slope of the change of inductor currents during the action of STVV and non-STVV can be calculated as:

$$k_{Lst} = \frac{i_{L1st}(k+1) - i_{L1}(k)}{T_s} \tag{13}$$

$$k_{Lnsti} = \frac{i_{L1nsti}(k+1) - i_{L1}(k)}{T_s} \tag{14}$$

where $i_{L1st}(k+1)$, k_{Lst} and $i_{L1nst}(k+1)$, k_{Lnsti} are predicted value and the slope of change of the i_{L1} under ST VV, predicted value and slope of change of i_{L1} under ST VV. Subscript $i = 1, 2, \ldots, 6$.

The predicted value of the i_{L1} under CVVs strategy through k_{Lst} and k_{Lnsti} is:

$$\begin{aligned} i'_{L1}(k+1) &= i_{L1}(k) + k_{Lst}T_s d_{sh} + k_{Lnsti}T_s(1-d_{sh}) \\ &= i_{L1\_ref} \end{aligned} \tag{15}$$

where $i'_{L1}(k+1)$, d_{sh}, i_{L1_ref} are the predicted value of the inductor current under the action of the CVVs, ST duty cycle, inductor current reference value.

Solving Eq. (15) yields the ST duty cycle under CVVs strategy as:

$$d_{sh} = \frac{i_{L1\_ref} - i_{L1}(k) - k_{Lnsti}T_s}{T_s(k_{Lst} - k_{Lnsti})} \tag{16}$$

The proposed method applies a composite voltage vector — including one shoot-through, one zero, and two active voltage vectors — to the QZSI during each sampling period. The active vectors are selected using a cost function. Firstly, a voltage vector quick selection table has been designed. Two adjacent voltage vectors are grouped together to synthesize desired voltage vectors of any amplitude within any sector (V_1 V_2; V_2; V_3; V_3 V_4; V_4; V_5; V_5 V_6; V_6; V_1). Secondly, from the ST duty cycle d_{sh}, the candidate set of voltage vectors is modulated, and the action times t_j, t_k, and t_0 of u_{optj}, u_{optk}, and the zero VV are calculated, respectively. Then, the combination of voltage vectors that decrease the error of dq-axis currents i_d, i_q and u_{C1} is computed by means of a cost function to obtain 2 active VVs u_{opt1} and u_{opt2} with their respective action times t_1, t_2. Finally, the optimal combination of modulated voltage vectors is applied to QZSI by generating switching signals via SVPWM.

The slopes of dq-axis currents at zero VV action, s_{q0} and s_{d0}, are calculated as:

$$\begin{cases} s_{q0} = -\dfrac{R_s i_q + \omega_e L_d i_d + \omega_e \psi_f}{L_q} \\ s_{d0} = \dfrac{-R_s i_d + \omega_e L_q i_q}{L_d} \end{cases} \tag{17}$$

From the above equation, the slopes of dq-axis currents when the active VV acts are $s_{qi} = s_{q0} + u_{qi}/L_q$ and $s_{di} = s_{d0} + u_{di}/L_d$, respectively. Subscript $i = 1, 2, \ldots, 6$. u_{di} and u_{qi} are the projections of the ith VV on the dq-axis coordinate system.

$$i'_d(k+1) = i_d(k) + s_{d0}(t_0 + d_{sh}T_s) + s_{dj}t_j + s_{dk}t_k = i_d^* \tag{18}$$

$$i'_q(k+1) = i_q(k) + s_{q0}(t_0 + d_{sh}T_s) + s_{qj}t_j + s_{qk}t_k = i_q^* \tag{19}$$

$$T_s = t_0 + t_j + t_k + d_{sh}T_s \tag{20}$$

where i_d^*, i_q^*, t_0, t_j, t_k are the reference value for the dq-axis current, duration of the action of zero VV, and two active VVs, respectively.

By solving Eqs. (18), (19), (20), t_0, t_j, and t_k are obtained as:

$$t_j = \frac{A+B}{E} \tag{21}$$

$$t_k = \frac{C+D}{E} \tag{22}$$

$$t_0 = T_s - t_j - t_k - d_{sh}T_s \tag{23}$$

$$\begin{cases} A = (i_d^* - i_d(k))(s_{qk} - s_{q0}) \\ \quad + (i_q^* - i_q(k))(s_{d0} - s_{dk}) \\ B = T_s(s_{q0}s_{dk} - s_{qk}s_{d0}) \\ C = (i_d^* - i_d(k))(s_{q0} - s_{qj}) \\ \quad + (i_q^* - i_q(k))(s_{dj} - s_{d0}) \\ D = T_s(s_{qj}s_{d0} - s_{q0}s_{dj}) \\ E = s_{q0}s_{dk} + s_{qj}s_{d0} + s_{qk}s_{dj} \\ \quad - s_{qj}s_{dk} - s_{qk}s_{d0} - s_{q0}s_{dj} \end{cases} \tag{24}$$

After calculating t_0, t_j, and t_k from Eqs. (21) to (24), the predicted values of dq-axis currents corresponding to the six desired VVs are obtained by substituting them into Eq. (12).

When ST VV and non-ST VV act, the change slope of capacitor voltage k_{Cst} and k_{Cnsti} is similar to the change slope of inductor current. It is important to note that the rate of change of the capacitor voltage u_{C1} differs depending on whether an STVV, zero VV, or active VV is applied. i_{inv} is 0 when the zero VV is acting, and the voltage change slope k_{C0} is then calculated by substituting the capacitor voltage prediction equation for non-ST times. The change slope of capacitor voltage and predicted value of capacitor voltage under CVVs strategy are

$$\begin{cases} k_{Cst} = \dfrac{u_{C1st}(k+1) - u_{C1}(k)}{T_s} \\ k_{Cnsti} = \dfrac{u_{C1nsti}(k+1) - u_{C1}(k)}{T_s} \end{cases} \tag{25}$$

$$\begin{aligned} u'_{C1}(k+1) &= u_{C1}(k) + k_{Cst}T_s d_{sh} + k_{Cnstj}t_j \\ &\quad + k_{Cnstk}t_k + k_{C0}t_0 \end{aligned} \tag{26}$$

This paper's non-STVV selection cost function differs from conventional predictive torque control by eliminating the need for i_L terms. This is achieved through dead-beat control of i_L, which decouples current regulation from the cost function. Under this circumstance, the proposed methodology's cost function incorporates only capacitor voltage u_{C1} and stator current tracking. Consequently, only u_{C1}'s weight coefficient requires design. This approach replaces traditional QZSI-based MPCC weighting of both u_{C1} and inductor current i_{L1}, significantly reducing coefficient calibration complexity. In this paper, weight coefficient λ_c of capacitor voltage term is designed to be 0.05. The cost function is expressed as:

$$\begin{aligned} g &= |i_d^* - i_d(k+1)| + \left|i_q^* - i_q(k+1)\right| \\ &\quad + \lambda_c \left|u_{C1\_ref} - u'_{C1}(k+1)\right| \end{aligned} \tag{27}$$

3.2. Sliding Mode Control Strategy of Speed Loop Based on NSMRL

The previously proposed QZSI-PMSM-MPCC method based on CVVs aims to decrease the i_L ripple and three-phase current pulsation in QZSI; however, PMSM suffers from the problem of unsatisfactory interference immunity when the external load of the system changes abruptly.

In order to realize high precision control of motor system speed, this paper combines the advantages of sliding mode control, which is less dependent on system accurate model and has good robustness, and the advantages of sliding mode disturbance observer, which has small vibration and high observation accuracy, and puts forward the sliding mode control of speed loop based on a novel reaching law.

The sliding mode control in this paper is divided into two parts, that is, sliding mode controller design and sliding mode perturbation observer design. The design of the improved sliding mode controller based on NSMRL is as follows. The state variables of the permanent magnet synchronous motor system are defined as:

$$\begin{cases} \boldsymbol{x}_1 = \omega_e^* - \omega_e \\ \boldsymbol{x}_2 = \dot{\boldsymbol{x}}_1 = -\dot{\omega}_e \end{cases} \tag{28}$$

where ω_e^* is the given electrical angular speed value, and ω_e is the actual electrical angular speed.

To smooth torque, reduce system errors, and minimize jitter, the following integral sliding mode surface is chosen:

$$\boldsymbol{s}_1 = \boldsymbol{x}_1 + \boldsymbol{c}\int_0^t \boldsymbol{x}_1 dt \tag{29}$$

where $\boldsymbol{c}$ is the integral coefficient of integral sliding surface.

Derivation of (29) yields:

$$\dot{\boldsymbol{s}}_1 = \dot{\boldsymbol{x}}_1 + \boldsymbol{c}\boldsymbol{x}_1 = \dot{\omega}_e^* - \omega_e + \boldsymbol{c}\boldsymbol{x}_1 \tag{30}$$

From Eqs. (9) and (10), the equation of state of the PMSM speed for parameter variations is derived as:

$$\frac{d\omega_e}{dt} = 1.5\frac{p_n^2}{J}\psi_{ect}i_q - \frac{B}{J}\omega_e + \frac{p_n}{J}(\Delta T_e - T_L) \tag{31}$$

where ψ_{ect}, ΔT_e are the active magnetic chain and change in load torque as the parameter changes, respectively.

Considering the internal parameter uptake of the system and the external load perturbation yields:

$$\frac{d\omega_e}{dt} = \alpha i_q - \frac{1}{J}d(t) - \frac{B}{J}\omega_e \tag{32}$$

where $\alpha = 3p_n\psi/2J$, $d_{(t)}$ represents the total system perturbation including internal parameter uptake and external load perturbation.

To resolve the convergence-chattering trade-off in conventional sliding mode reaching laws, this paper proposes a state-dependent adaptive reaching law. Based on the exponential reaching law framework, this method dynamically adjusts its gain parameters according to sliding surface distance and system state variations.

$$\begin{cases} \dot{\boldsymbol{s}}_1 = -f(\boldsymbol{x}_1, \boldsymbol{s}_1)\mathrm{sgn}(\boldsymbol{s}) - \boldsymbol{k}_1\boldsymbol{s}_1 \\ f(\boldsymbol{x}_1, \boldsymbol{s}_1) = \dfrac{\varepsilon\,|\boldsymbol{x}_1|}{\boldsymbol{k}_2 + (1-\boldsymbol{k}_2)e^{-\delta|\boldsymbol{s}_1|}} \\ \lim\limits_{t\to 0}|\boldsymbol{x}_1| = 0,\ \varepsilon > 0,\ \boldsymbol{\delta} > 0,\ \boldsymbol{k}_1 > 0,\ 0 < \boldsymbol{k}_2 < 1 \end{cases} \tag{33}$$

In combination with Eq. (32) and Eq. (33), a sliding mode control law is formulated as follows:

$$i_q^* = \boldsymbol{\alpha}^{-1}\left[\frac{B}{J}d(t) + \boldsymbol{c}\boldsymbol{x}_1 + f(\boldsymbol{x}_1, \boldsymbol{s}_1)\mathrm{sgn}(\boldsymbol{s}_1) + \boldsymbol{k}_1\boldsymbol{s}_1\right] \tag{34}$$

From Eq. (34), the sign function is included in the sliding mode controller. To further decrease jitter, we use sigmoid functions instead of the sign function as follows:

$$sigmoid(\boldsymbol{s}) = \frac{2}{1+e^{-2\boldsymbol{s}}} - 1 \tag{35}$$

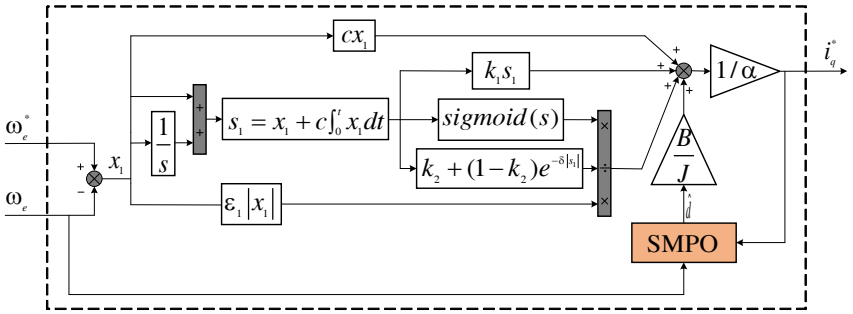

FIGURE 4. Block diagram of the NSMRL based controller.

In summary, the block diagram of the NSMRL based controller is shown in Fig. 4.

Proof 1: The Lyapunov function V is chosen as:

$$V = \frac{1}{2}\boldsymbol{s}^2 \tag{36}$$

Derivation of (36) and combining (33) yields:

$$\begin{aligned}\dot{V} &= \boldsymbol{s_1}\dot{\boldsymbol{s}}_{\boldsymbol{1}} \\ &= \boldsymbol{s_1}\left[\boldsymbol{c}\boldsymbol{x_1} + \dot{\omega}_e^* - \left(\boldsymbol{\alpha} i_q^* - \frac{1}{J}d(t) - \frac{B}{J}\omega_e\right)\right] \\ &= \boldsymbol{s_1}\left[-f(\boldsymbol{x_1}, \boldsymbol{s_1})\mathrm{sgn}(\boldsymbol{s_1}) - \boldsymbol{k_1 s_1}\right] \\ &= -f(\boldsymbol{x_1}, \boldsymbol{s_1})\,|\boldsymbol{s_1}| - \boldsymbol{k_1 s_1^2} \le 0\end{aligned} \tag{37}$$

According to Lyapunov stability theory, the system with this sliding mode controller is stable, and the error of tracking will tend to zero in a limited amount of time.

The design of sliding mode perturbation observer based on NSMRL is as follows. In order to further improve the system's perturbation resistance, a sliding mode perturbation observer is designed. Taking mechanical angular velocity ω_e and total system perturbations $d_{(t)}$ as status variations, the magnetic torque T_e as the system input, and mechanical angular velocity observation as the system output, sliding mode observer equation can be obtained as:

$$\begin{cases}\boldsymbol{e_\omega} = \omega_e - \hat{\omega}_e \\ \boldsymbol{e_T} = d - \hat{d}\end{cases} \tag{38}$$

where $\boldsymbol{e_\omega}$, $\boldsymbol{e_T}$, $\hat{d}$ are velocity observation error, perturbation observation error, and observed values of external load disturbances.

$$\begin{cases}\dot{\hat{\omega}}_e = -\dfrac{B}{J}\omega_e - \dfrac{1}{J}\hat{d} + \dfrac{1}{J}T_e + g(\boldsymbol{e_\omega}) \\ \dot{\hat{d}} = \boldsymbol{l}g(\boldsymbol{e_\omega})\end{cases} \tag{39}$$

where $\boldsymbol{l}$, $g_{(}\boldsymbol{e_\omega})$ are observer gain and sliding mode control law corresponding to the velocity observation error.

From Eqs. (28) and (39), error equation of perturbed observer is given as:

$$\begin{cases}\dot{\boldsymbol{e}}_{\boldsymbol{\omega}} = -\dfrac{B}{J}\boldsymbol{e_\omega} - \dfrac{1}{J}\boldsymbol{e_T} - g(\boldsymbol{e_\omega}) \\ \dot{\boldsymbol{e}}_{\boldsymbol{T}} = -\boldsymbol{l}g(\boldsymbol{e_\omega})\end{cases} \tag{40}$$

The integral slip mode surface is selected as:

$$\boldsymbol{s_\omega} = \boldsymbol{e_\omega} + \boldsymbol{c_\omega}\int_0^t \boldsymbol{e_\omega} dt \tag{41}$$

Derivation of (41) yields:

$$\dot{\boldsymbol{s}}_{\boldsymbol{\omega}} = \dot{\boldsymbol{e}}_{\boldsymbol{\omega}} + \boldsymbol{c_\omega}\boldsymbol{e_\omega} \tag{42}$$

The reaching law is chosen as:

$$\dot{\boldsymbol{s}}_{\boldsymbol{\omega}} = -\boldsymbol{k_s}\mathrm{sgn}(\boldsymbol{s_\omega}) \tag{43}$$

where $\boldsymbol{s_\omega}$ is the sliding mold surface, and $\boldsymbol{k_s}$ is the switching gain.

Combining Eqs. (38) to (40) and also considering $-e_T/J$ as a perturbation term, the control law of sliding mode perturbation observer is designed:

$$g(\boldsymbol{e_\omega}) = \left(\boldsymbol{c_\omega} - \frac{B}{J}\right)\boldsymbol{e_\omega} + \boldsymbol{k_s}\mathrm{sgn}(\boldsymbol{s_\omega}) \tag{44}$$

In summary, the control block diagram of the improved perturbation observer is shown in Fig. 5.

Proof 2: The Lyapunov function V is chosen as:

$$V = \frac{1}{2}\mathbf{s}_\omega^2 \tag{45}$$

Derivation of (45) yields:

$$\begin{aligned}\dot{V} &= \boldsymbol{s_\omega}\dot{\boldsymbol{s}}_{\boldsymbol{\omega}} \\ &= \boldsymbol{s_\omega}\left[\boldsymbol{c_\omega}\boldsymbol{e_\omega} - \frac{B}{J}\boldsymbol{e_\omega} - \frac{1}{J}\boldsymbol{e_T} - g(\boldsymbol{e_\omega})\right] \\ &= \boldsymbol{s_\omega}\left[-\boldsymbol{k_s}\mathrm{sgn}(s_\omega) - \frac{1}{J}\boldsymbol{e_T}\right] < 0\end{aligned} \tag{46}$$

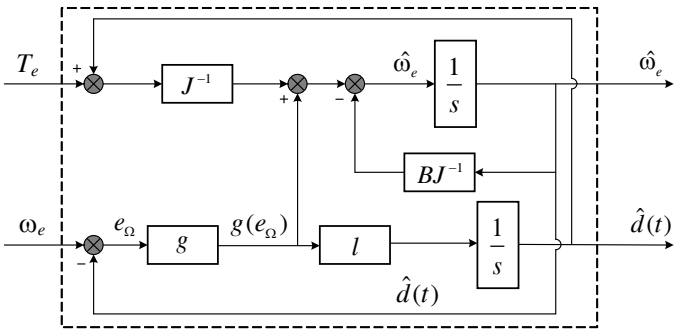

FIGURE 5. Control block diagram of the disturbance observer.

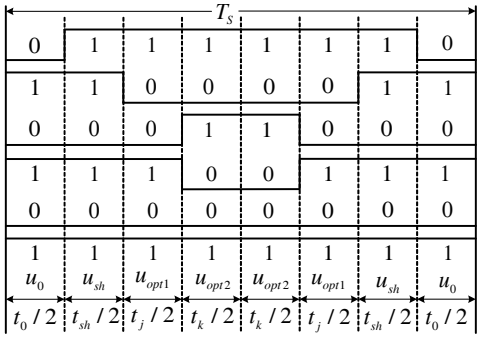

FIGURE 6. The diagram of driving pulse.

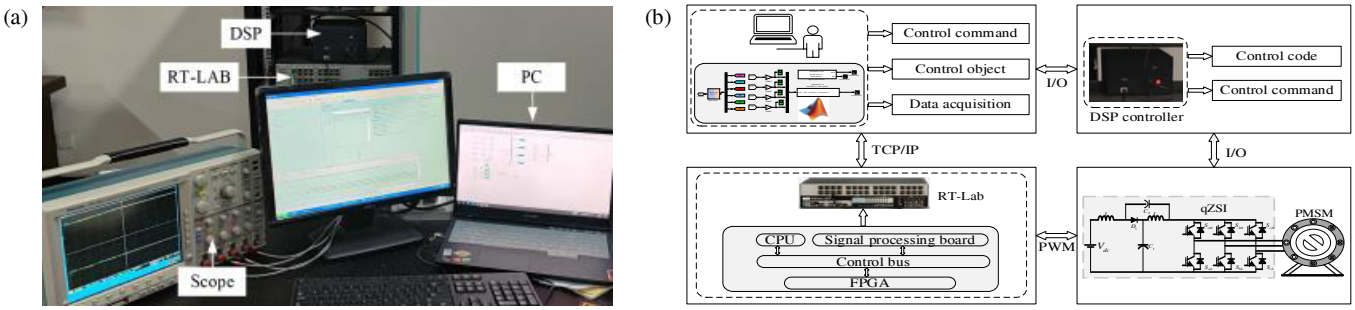

FIGURE 7. Experimental platform. (a) RT-LAB experimental platform. (b) RT-LAB in-the-loop system configuration.

According to Lyapunov stability theory, in order to make the system sliding mode surface stability tends to zero, from Equation (46) $\mathbf{k_s}$ should be designed to satisfy:

$$\boldsymbol{k_s} > \boldsymbol{l}\frac{|\boldsymbol{e_T}|}{J} \tag{47}$$

where $\boldsymbol{l}$ is a constant bigger than 1. When the load disturbance observation error $\boldsymbol{e_T}$ is large, the switching gain $\boldsymbol{k_s}$ increases accordingly to ensure the robustness of the system. When $\boldsymbol{e_T}$ tends to 0, the switching gain $\boldsymbol{k_s}$ also tends to 0 to weaken the sliding mode jitter phenomenon of the observation.

3.3. Switching Frequency Analysis

Using multiple VVs in one control cycle increases the inverter switching frequency, so the switching frequency of proposed CVVs strategy is analyzed here. This paper uses a seven-stage SVPWM algorithm to flexibly select ST VV and zero VV when using different non-STVVs to change the switching state of the switching tube, and only change the switching state of one phase to reduce switching loss. Taking the first set of voltage vectors V_1 and V_2 as an example, zero VV, STVV, and active VV are applied sequentially, and the voltage vectors are evenly distributed in time. The total switching count per control cycle reaches 8 actions—2 additional actions compared to conventional SVM dual-vector strategies due to STVV implementation. Nevertheless, the CVVs strategy not only expands the voltage vector selection range but also enhances QZSI performance without significantly increasing switching losses. The modulation strategy of the proposed scheme is illustrated in Fig. 6.

4. EXPERIMENTAL RESULTS AND ANALYSIS

Proposed CVVs-NSMRL-MPCC strategy is experimentally validated using RT-LAB experimental platform shown in Fig. 7. TMS320F2812 was used as the digital signal processing (DSP) controller, and RT-LAB (op5600) was used to build the system, inverter, and other parts of the PMSM. The experimental system captures data at 10 kHz. Firstly, the superiority of the CVVs strategy proposed in this paper is verified. Secondly, the anti-load disturbance performance of the PMSM side is verified. Since there are fewer QZSI based PMSM model prediction strategy in the literature for improving the anti-disturbance performance of PMSM side, CVVs-PI-MPCC control strategy is used in this paper as comparison. The various parameters of PMSM and QZSI used therein are shown in Table 2. Conventional quasi-Z-source SVM strategy and CVVs-PI-MPCC strategy control parameters are $k_p = 10$, $k_i = 100$. The parameters of the proposed CVVs-NSMRL-MPCC strategy to control the sliding mode are $\alpha = 0.001$, $c = 200$, $\varepsilon = 0.01$, $\sigma = 100$, $k_1 = 200$, $k_2 = 0.001$.

4.1. Steady State Experiment

The given working conditions are as follows: QZSI-PMSM was operated under the operating conditions of 1000 r/min rotational speed and 15 N·m load torque. Reference value for u_C is 225 V, while the given reference value for V_{dc} is 300 V. The steady-state experimental waveforms of the three control strategies are shown in Figs. 8–9.

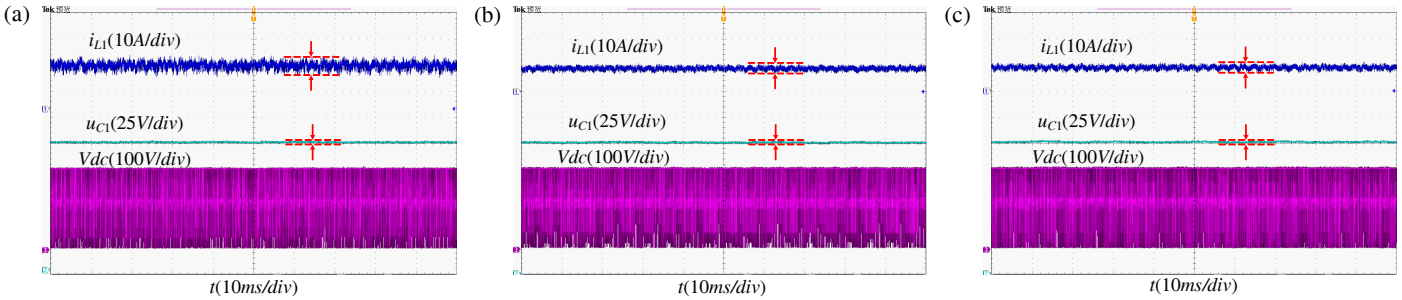

FIGURE 8. Experimental waveforms of QZSI side steady-state. (a) SVM based QZSI strategy. (b) CVVs based QZSI strategy. (c) CVVs-NSMRL-MPC strategy.

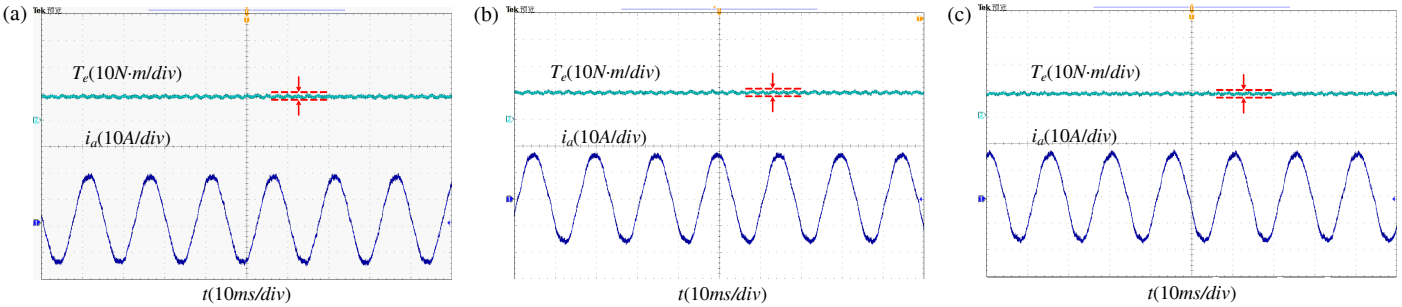

FIGURE 9. Experimental waveforms of PMSM side steady-state. (a) SVM based QZSI strategy. (b) CVVs based QZSI strategy. (c) CVVs-NSMRL-MPC strategy.

TABLE 2. PMSM and QZSI parameters.

Parameters and Unit	Values
Stator resistance (Ω)	0.15
Stator inductance (mH)	1.625
Rotational inertia (kg·m^2)	4.78e-3
PM flux linkage (Wb)	0.1
Number of pole pairs	4
Rated speed (r/min)	1000
Rated torque (N·m)	15
DC Source Voltage (V)	150
QZSI Capacitor (μF)	470
QZSI Inductor (mH)	2

Comparing Fig. 8(b) with Fig. 8(a), it can be observed that the steady-state ripple of i_{L1} on QZSI side decreases when the CVVs strategy is used, and the u_{C1} ripple is slightly reduced. Comparing Fig. 9(b) with Fig. 9(a), the proposed CVVs strategy has lower three-phase current waveform distortion rate. Table 3 shows the superiority of the proposed CVVs strategy more visually. Compared with the traditional SVM strategy, the proposed CVVs strategy reduces the i_{L1} ripple by about 40.94% and the u_{C1} ripple by about 13.14% on the QZSI side, and reduces the THD by about 32.75% on the PMSM side in the steady-state experiments. The CVVs-NSMRL-MPC strategy exhibits similar steady-state performance to the CVVs-based QZSI strategy.

4.2. Transient State Experiment

After verifying the superiority of the steady-state performance of the proposed CVVs control strategy, the dynamic performance is compared when load torque and speed are varied. Under the variable speed condition, the reference value of u_{C1} is set to 225 V, the motor load set to 15 N·m, and the motor speed incremented from the reference value of 1000 r/min to 1400 r/min, and then decremented to 1000 r/min. Comparing Figs. 10(a) and (b), under the transient speed variations, the u_{C1} and V_{dc} fluctuations on the QZSI side of the CVVs-NSMRL-MPC strategy are smaller, and the transient process times of i_{L1} and u_{C1} are substantially reduced as compared to that of the CVVs-based QZSI strategy. As shown in Figs. 11(a) and (b), under transient speed variations, the CVVs-NSMRL-MPC strategy achieves an 18.59% reduction in response time during speed surges and a 73.73% reduction during speed sags, outperforming the CVVs-based QZSI strategy. Meanwhile, the torque pulsation under the CVVs-NSMRL-MPC strategy is smaller, which is reduced by 22.54% in comparison. It can be seen that the proposed CVVs-NSMRL-MPC strategy has a faster dynamic performance response speed than the CVVs without sliding mode. Table 4 shows the superiority of the proposed CVVs-NSMRL-MPC strategy more visually.

Under the variable torque condition, the reference value of u_{C1} is set to 225 V; the reference value of the motor speed is 1000 r/min; and the motor load torque is incremented from 15 N·m to 20 N·m, and then decremented to 15 N· m. As can be seen by comparing Figs. 12(a) and (b), under transient speed variations the two strategies have similar control effects on the QZSI side. In comparison with Figs. 13(a) and (b), it can be

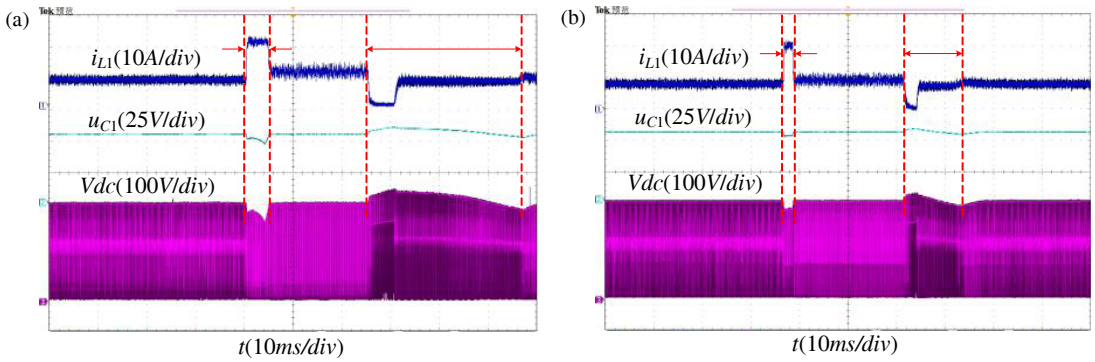

FIGURE 10. Experimental waveforms of QZSI side at variable speed. (a) CVVs based QZSI strategy. (b) CVVs-NSMRL-MPC strategy.

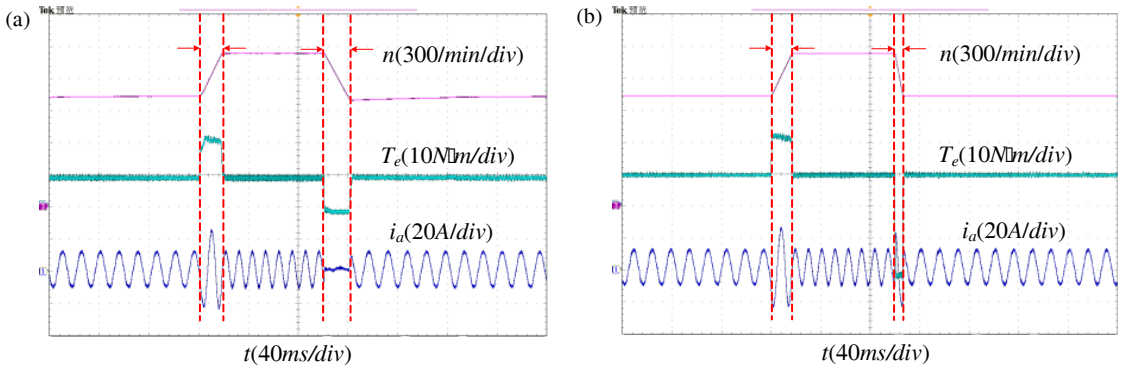

FIGURE 11. Experimental waveforms of PMSM side at variable speed. (a) CVVs based QZSI strategy. (b) CVVs-NSMRL-MPC strategy.

TABLE 3. Steady-state experimental results of multiple control variables.

Control variables	SVM based QZSI strategy	CVVs based QZSI strategy	CVVs-NSMRL-MPC strategy
Δi_L (A)	6.62	3.91	3.93
Δu_c (V)	2.41	2.13	2.21
ΔT_e (N·m)	2.15	1.95	1.93
i_a THD (%)	4.61	3.10	2.95

TABLE 4. Transient-state experimental results at variable speed.

Dynamic changes	CVVs based QZSI strategy	CVVs-NSMRL-MPC strategy
n (1000 $\rightarrow$ 1400 r/min)	34.53 ms	28.11 ms
n (1400 $\rightarrow$ 1000 r/min)	27.41 ms	7.20 ms
ΔT_e (N·m)	2.75	2.13

TABLE 5. Transient-state experimental results at variable load torque.

Dynamic changes	CVVs based QZSI strategy	CVVs-NSMRL-MPC strategy
T_e (10 $\rightarrow$ 15 N·m)	2.10 ms	1.96 ms
T_e (15 $\rightarrow$ 10 N·m)	2.53 ms	2.45 ms
T_e (N·m)	2.67	2.33

seen that under transient load torque variations, the response time of the CVVs-NSMRL-MPC strategy is 6.67% shorter during the load torque surge and 3.16% shorter during the load torque drop, which is better than that of the CVVs-based QZSI strategy. Meanwhile, the torque pulsation under the CVVs-NSMRL-MPC strategy is less, which is reduced by 12.73% in comparison. Table 5 shows the superiority of the proposed CVVs-NSMRL-MPC strategy more visually.

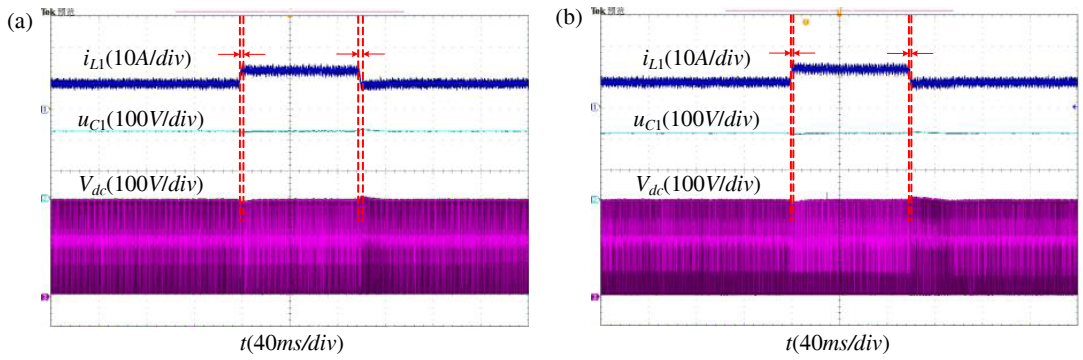

FIGURE 12. Experimental waveforms of QZSI side at variable load torque. (a) CVVs based QZSI strategy. (b) CVVs-NSMRL-MPC strategy.

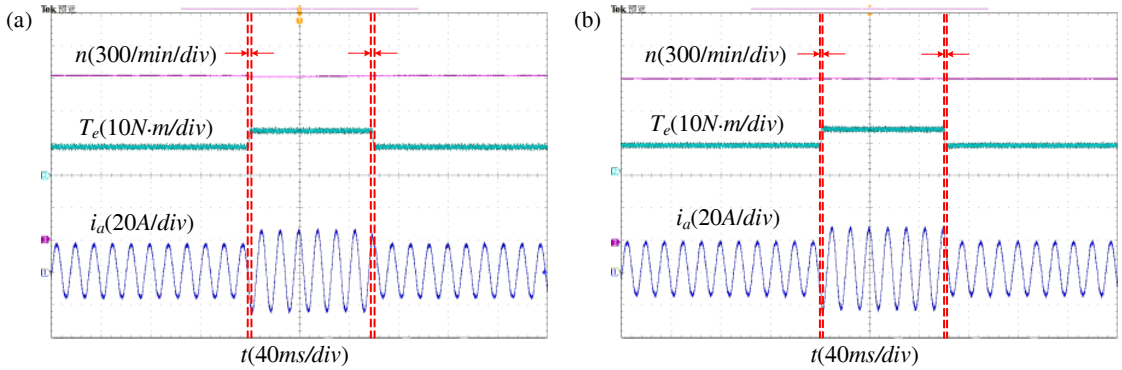

FIGURE 13. Experimental waveforms of PMSM side at variable load torque. (a) CVVs based QZSI strategy. (b) CVVs-NSMRL-MPC strategy.

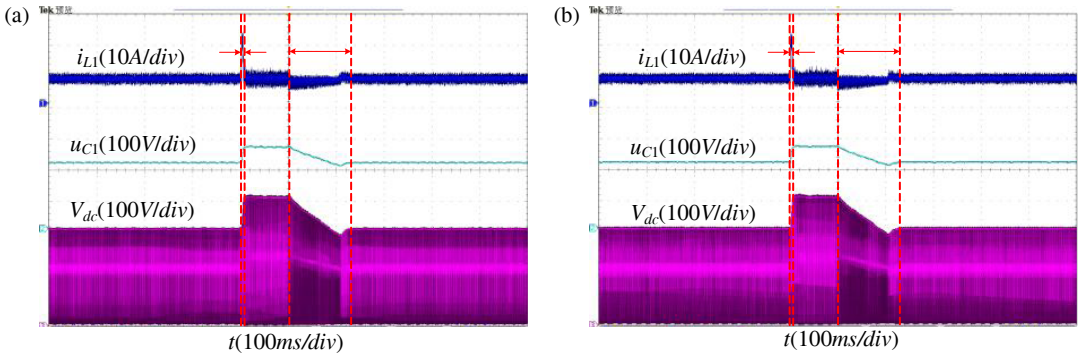

FIGURE 14. Experimental waveforms of PMSM side at variable DC bus voltage. (a) CVVs based QZSI strategy. (b) CVVs-NSMRL-MPC strategy.

4.3. Transient State Performance Verification of QZSI Network

This part of the experiment is to verify the dynamic response of the proposed CVVs-NSMRL-MPC strategy when the DC bus voltage varies. The control performance of QZSI side of proposed control strategy is verified for the sudden change of the given reference values of u_C and V_{DC}. The motor speed is kept constant at 1000 r/min, and load torque is constant at 15 N·m. The corresponding V_{DC} at the output of the inverter rises from 300 V to 400 V and falls from 400 V to 300 V. As depicted in Fig. 14, the two control strategies demonstrate comparable transient response characteristics. Under abrupt step increases in the commanded capacitor voltage, both u_C and V_{DC} exhibit rapid tracking responses to the reference variation. Conversely, during voltage step reductions, the system requires finite recovery duration to regain steady-state operation, primarily attributed to the inherent slow discharge dynamics of the capacitive elements.

5. CONCLUSION

Aiming at the problems of large ripples of inductor current and motor stator current in QZSI-based PMSM system, as well as the system's susceptibility to load torque disturbance. A QZSI

composite voltage vector model predictive current control strategy with a novel sliding mode reaching law is proposed. The proposed method improves the control performance and anti-interference performance of the system. Through the experimental analysis for different operating conditions, conclusion of the suggested control strategy is given as follows.

1) Compared to conventional SVM strategy, the u_C is more stable, and V_{DC} pulsation is smaller in proposed CVVs-QZSI strategy because composite voltage vector is applied. The i_L ripple on the QZSI side is reduced by 40.94% and the stator current waveform distortion rate of PMSM reduced by 32.75%.

2) In the proposed CVVs-QZSI strategy, the i_L term can be omitted from the cost function during active voltage vector selection. This simplification reduces weighting coefficient calibration complexity.

3) The NSMRL-based sliding mode controller and disturbance observer effectively suppress motor speed jitter and torque pulsation under external load variations. Compared with CVVs-PI-MPC, the proposed CVVs-NSMRL-MPCC strategy achieves significantly improved dynamic response during variable-speed operation.

ACKNOWLEDGEMENT

This work was supported by the Scientific Research Fund of Hunan Provincial Education Department under Grant Number 24A0395.

REFERENCES

[1] Peng, F. Z., "Z-source inverter," *IEEE Transactions on Industry Applications*, Vol. 39, No. 2, 504–510, Mar.-Apr. 2003.

[2] Anderson, J. and F. Z. Peng, "Four quasi-Z-source inverters," in *2008 IEEE Power Electronics Specialists Conference*, 2743–2749, Rhodes, Greece, 2008.

[3] Liu, Y., B. Ge, H. Abu-Rub, and F. Z. Peng, "Overview of space vector modulations for three-phase Z-source/quasi-Z-source inverters," *IEEE Transactions on Power Electronics*, Vol. 29, No. 4, 2098–2108, Apr. 2014.

[4] Grgić, I., M. Bašić, D. Vukadinović, and I. Marinović, "Novel space-vector PWM schemes for enhancing efficiency and decoupled control in quasi-Z-source inverters," *Energies*, Vol. 17, No. 6, 1387, 2024.

[5] Gong, R., G. Zhan, X. Zhang, and J. Liu, "A novel hybrid quasi-Z-source inverter topology and its modulation strategy," *Electrical Engineering*, Vol. 105, No. 2, 1067–1077, 2023.

[6] Do, T. V., M. Kandidayeni, J. P. F. Trovão, and L. Boulon, "Dual-source high-performance active switched quasi-Z-source inverter for fuel cell hybrid vehicles," *IEEE Transactions on Power Electronics*, Vol. 38, No. 10, 12 497–12 507, Oct. 2023.

[7] Liu, Y. and J. J. Li, "High precision model predictive power control method for battery energy-stored quasi Z-source inverter," *IEEE Transactions on Power Electronics*, Vol. 39, No. 8, 9481–9489, Aug. 2024.

[8] Zhang, Y., S. Li, Y. Liu, Z. Tang, and B. Luo, "Unconstrained optimization MPC method for qZSI-VSG grid-connected wind power system," *International Journal of Electrical Power & Energy Systems*, Vol. 162, 110276, 2024.

[9] Gu, Y., Y. Chen, and B. Zhang, "Enhanced-boost quasi-Z-source inverter with an active switched Z-network," *IEEE Transactions on Industrial Electronics*, Vol. 65, No. 10, 8372–8381, Oct. 2018.

[10] Young, H. A., M. A. Perez, J. Rodriguez, and H. Abu-Rub, "Assessing finite-control-set model predictive control: A comparison with a linear current controller in two-level voltage source inverters," *IEEE Industrial Electronics Magazine*, Vol. 8, No. 1, 44–52, Mar. 2014.

[11] Yu, B., W. Song, K. Yang, Y. Guo, and M. S. R. Saeed, "A computationally efficient finite control set model predictive control for multiphase PMSM drives," *IEEE Transactions on Industrial Electronics*, Vol. 69, No. 12, 12 066–12 076, Dec. 2022.

[12] Yu, B., W. Song, Y. Guo, and M. S. R. Saeed, "A finite control set model predictive control for five-phase PMSMs with improved DC-link utilization," *IEEE Transactions on Power Electronics*, Vol. 37, No. 3, 3297–3307, Mar. 2022.

[13] Luo, Y. and C. Liu, "Multi-vector-based model predictive torque control for a six-phase PMSM motor with fixed switching frequency," *IEEE Transactions on Energy Conversion*, Vol. 34, No. 3, 1369–1379, Sep. 2019.

[14] Yang, H., M. Li, Y. Zhang, and A. Xu, "FCS-MPC for three-level NPC inverter-fed SPMSM drives without information of motor parameters and DC capacitor," *IEEE Transactions on Industrial Electronics*, Vol. 71, No. 4, 3504–3513, Apr. 2024.

[15] Li, T., X. Sun, G. Lei, Y. Guo, Z. Yang, and J. Zhu, "Finite-control-set model predictive control of permanent magnet synchronous motor drive systems — An overview," *IEEE/CAA Journal of Automatica Sinica*, Vol. 9, No. 12, 2087–2105, Dec. 2022.

[16] Brosch, A., O. Wallscheid, and J. Böcker, "Long-term memory recursive least squares online identification of highly utilized permanent magnet synchronous motors for finite-control-set model predictive control," *IEEE Transactions on Power Electronics*, Vol. 38, No. 2, 1451–1467, Feb. 2023.

[17] Li, X., Z. Xue, X. Yan, *et al.*, "Voltage vector rapid screening-based three-vector model predictive torque control for permanent magnet synchronous motor," *Transactions of China Electrotechnical Society*, Vol. 37, No. 7, 1666–1678, 2022.

[18] Ismeil, M. A., O. Abdel-Rahim, H. S. Hussein, and E. H. Abdelhameed, "Implementation of new optimal control methodology of quazi Z-source inverter based on MPC," *IEEE Access*, Vol. 11, 56 453–56 462, 2023.

[19] Bakeer, A., M. A. Ismeil, and M. Orabi, "A powerful finite control set-model predictive control algorithm for quasi Z-source inverter," *IEEE Transactions on Industrial Informatics*, Vol. 12, No. 4, 1371–1379, Aug. 2016.

[20] Mahmoudi, H., M. Aleenejad, and R. Ahmadi, "Modulated model predictive control for a Z-source-based permanent magnet synchronous motor drive system," *IEEE Transactions on Industrial Electronics*, Vol. 65, No. 10, 8307–8319, 2017.

[21] Mahmoudi, H., M. Aleenejad, and R. Ahmadi, "Torque ripple minimization for a permanent magnet synchronous motor using a modified quasi-Z-source inverter," *IEEE Transactions on Power Electronics*, Vol. 34, No. 4, 3819–3830, Apr. 2019.

[22] Dong, K., T. Shi, S. Xiao, X. Li, and C. Xia, "Finite set model predictive control method for quasi-Z source inverter-permanent magnet synchronous motor drive system," *IET Electric Power Applications*, Vol. 13, No. 3, 302–309, 2019.

[23] Ahmed, A. A., A. Bakeer, H. H. Alhelou, P. Siano, and M. A. Mossa, "A new modulated finite control set-model predictive control of quasi-Z-source inverter for PMSM drives," *Electronics*, Vol. 10, No. 22, 2814, 2021.

[24] Zhang, Y., K. Cao, W. Yi, Y. Meng, and Z. Cheng, "Three-phase duty cycle modulation-based model predictive control strategy for QZSI-PMSM system without cost function," *Progress In Electromagnetics Research C*, Vol. 148, 205–217, 2024.

[25] Liu, J. and X. Wang, "Discrete sliding mode control," in *Advanced Sliding Mode Control for Mechanical Systems*, 97–110, Tsinghua University Press, 2012.

[26] Bakeer, A., M. A. Ismeil, and M. Orabi, "Modified finite control set-model predictive controller (MFCS-MPC) for quasi Z-source inverters based on a current observer," *Journal of Power Electronics*, Vol. 17, No. 3, 610–620, 2017.

[27] Rahmatullah, R., A. Ak, and N. F. O. Serteller, "Design of sliding mode control using SVPWM modulation method for speed control of induction motor," *Transportation Research Procedia*, Vol. 70, 226–233, 2023.

[28] Abid, A., A. Bakeer, H. Albalawi, M. Bouzidi, A. Lashab, A. Chub, and S. A. Zaid, "Model-free predictive control for improved performance and robustness of three-phase quasi Z-source inverters," *IEEE Access*, Vol. 12, 87 850–87 863, 2024.

[29] Peng, F., W. Xie, and J. Yan, "Compound robust control of permanent magnet synchronous motor based on quasi-Z source inverter," *IET Electric Power Applications*, Vol. 17, No. 7, 893–905, 2023.

[30] Mahmoudi, H., M. Aleenejad, P. Moamaei, and R. Ahmadi, "Fuzzy adjustment of weighting factor in model predictive control of permanent magnet synchronous machines using current membership functions," in *2016 IEEE Power and Energy Conference at Illinois (PECI)*, 1–5, Urbana, IL, USA, Feb. 2016.